The Effects of Focal Articular Defects on Cartilage Contact Mechanics

Kenneth R. Gratz,[1] Benjamin L. Wong,[1] Won C. Bae,[2] Robert L. Sah[1,3,4]

[1]Departments of Bioengineering, University of California–San Diego, 9500 Gilman Drive, Mail Code 0412, La Jolla, California 92093-0412, [2]Department of Radiology, University of California–San Diego, 9500 Gilman Drive, La Jolla, California 92093-0412, [3]Stein Institute for Research on Aging, La Jolla, California, [4]Whitaker Institute of Biomedical Engineering, University of California–San Diego, La Jolla, California

ABSTRACT: Focal damage to articular cartilage is common in arthroscopy patients, and may contribute to progressive tissue degeneration by altering the local mechanical environment. The effects of a focal defect, which may be oriented at various orientations relative to the subchondral bone, on the dynamics of cartilage contact and deformation are unclear. The objective of this study was to elucidate the effect of experimental full thickness focal defects, oriented at 80° or 100° relative to the subchondral bone, on intratissue strain and surface sliding of opposing cartilage surfaces during compression and stress relaxation. Pairs of intact bovine osteochondral blocks were compressed uniaxially by 20%, and allowed to stress relax. Tissue deformation was recorded by video microscopy. A full-thickness defect (with either 80° or 100° edges) was created in one block from each pair. Blocks were allowed to reswell and retested. Defect edges were then recut with the opposite orientation, allowed to reswell, and retested again. Stained nuclei were tracked by digital image correlation and used to quantify cartilage strains and surface sliding. The results indicated that loading of intact samples caused axial strain magnitudes that decreased with depth and relatively little sliding. With loading of samples containing defects, strain magnitudes were elevated in cartilage adjacent to, and opposing, defects. For samples with edge orientations of 100°, sliding magnitudes were increased over surfaces adjacent to defects. These local mechanical changes due to full-thickness articular cartilage defects may contribute to altered chondrocyte metabolism, tissue damage, or accelerated wear. © 2008 Orthopaedic Research Society. Published by Wiley Periodicals, Inc. J Orthop Res 27:584–592, 2009

Keywords: cartilage; focal defect; biomechanics; contact mechanics

Focal defects in articular cartilage are commonly found in symptomatic knees,[1,2] and may be implicated in the progressive degeneration of cartilage.[3–7] Although the exact mechanism by which defects contribute to cartilage damage have not been elucidated, prior studies have suggested a mechanical role in this process.

A variety of excessive mechanical loading protocols have been shown to result in both matrix damage[8–12] and cell death.[8,9,11,13–17] The exact conditions initiating this damage remain to be established, but excessive strain magnitudes[18] and rates[9] both appear to contribute. Over time, even moderate increases in load may be expected to accelerate the rates of both mechanical fatigue[19–21] and wear.[22,23] Additionally, changes in the magnitudes or dynamics of cartilage loading may affect the cellular response of the tissue,[24] and in the long term, regulate the processes of tissue growth and remodeling.[25] Changes to the dynamic tissue response to loading that may occur with a defect could significantly contribute to tissue damage or altered cellular activity.

The effects of focal defects on the mechanical environment of articular cartilage have been predicted theoretically and analyzed experimentally in in vitro systems. Peak and average contact stresses and contact stress gradients are increased along surfaces adjacent to the rim of a focal defect.[26,27] However, the loss of contact area at a defect site is offset by the radial recruitment of new contact area, helping to limit increases in contact stresses.[26] Increased macroscopic tissue deformation is necessary for this load redistribution to occur, and has been observed in the cartilage surrounding and opposing

focal defects in histological sections of loaded joints.[28] Additionally, theoretical models of cartilage contact have predicted that lower congruity between contacting surfaces will result in a decrease in fluid support and thus greater loading on the solid matrix;[29] and finite element models of joints with focal defects, that predict increases in contact stresses consistent with ex vivo experimental measurements, predict increased strains in the tissue adjacent to a defect.[30] However, quantitative experimental measurements of the deformations near defects have not yet been performed, and it is unclear whether strain magnitudes approach levels associated with injury.

Several past studies have measured intratissue cartilage strains under a variety of loading conditions by optically tracking cell nuclei.[31–35] More recently, these methods were extended to investigate the contact of two independent cartilage surfaces subjected to uniaxial compression[36] or relative motion and sliding,[37] quantifying cartilage strain during loading. Image analyses were introduced to allow dynamic deformation of contacting cartilage surfaces to be automatically tracked, and a detailed mathematical framework to describe the contact between the surfaces was presented.[36] Building on those methods will allow in-depth studies of cartilage contact in both normal and diseased states to be performed.

The hypothesis of the current study is that, in addition to affecting intratissue strain distributions directly following loading, the presence of a defect alters the time course of strain development and surface sliding during loading and the subsequent redistribution of strain during relaxation. Thus, the objectives were to (1) compare the distribution of intratissue strains during compression and stress relaxation of opposing intact, and defect-containing, cartilage samples; and (2) determine the effect of defect presence and edge orientation on the

Correspondence to: Robert L. Sah (T: 858-534-0821; F: 858-822-1614; E-mail: rsah@ucsd.edu)

sliding between contacting surfaces. This represents the first experimental study of dynamic cartilage contact near defects and the complex sliding over the defect rim. Knowledge of changes in the mechanical environment arising near a focal defect could help to identify tissue regions susceptible to damage and validate theoretical models of cartilage contact.

MATERIALS AND METHODS

Study Design
Pairs of intact osteochondral blocks ($n = 4$) were mechanically tested, as a normal control. Following testing, a single, 4 mm wide, full-thickness defect was created in one block from each pair. Defect edges were cut with either an "open" ($\sim100°$) or "closed" ($\sim80°$) orientation, with respect to the defect base (Fig. 1A). The orientation of the edge was determined as that of the line connecting the points on the edge at the defect base and rim. Samples were allowed to reequilibrate >1 h in bovine synovial fluid (SF) with the addition of protease inhibitors (PIs),[38] and retested using the same protocol. The defect edge was then recut with the opposite orientation (closed to open, and vice versa); samples were again allowed to reequilibrate >1 h in SF + PIs and retested a final time. The initial defect orientation was randomly chosen for each sample.

Sample Preparation
Macroscopically normal osteochondral blocks ($10 \times 10 \times 2.5$ mm^3; L × W × H) with smooth, intact surfaces were harvested from the femoral condyles of mature bovine knees (Fig. 1A). Blocks were soaked in phosphate-buffered saline (PBS) containing PIs and stored at $-70°$C until testing. Blocks were thawed by immersion in PBS + PIs, stained (cell nuclei) for >4 h at 4°C with 20 µg/mL propidium iodide in PBS + PIs, and then equilibrated for 12 h at 4°C in SF + PIs, to provide hydration of the tissue and lubrication of the surface boundary.[37] Prior to testing, cartilage thickness was optically measured at five places spanning the sample width; sample

Figure 1. Sample preparation (A) and micromechanical testing (B) of opposing osteochondral blocks.

thickness was determined as the average of these five measurements. Blocks obtained from the same knee were tested against each other to closely match the mechanical properties.

Full-thickness articular cartilage defects extending to the calcified cartilage layer were created in "open" and "closed" orientations by making a series of incisions in the cartilage. To make the initial defect, three incisions were made. First, a cut was made perpendicular to the surface at the center of the sample width. Second, the two edges of the defect were cut at the desired angle at 2 mm (at their center) to each side of the initial cut. Third, the cartilage was undercut along the bone starting at the center incision and cutting towards each edge until the cartilage released. Subsequently, for the second test with the defect in the other orientation, a cut was made relative to the defect point that was furthest from the defect center (located at either the base or rim). This additional incision resulted in a small increase [0.35 mm (+9%), for a cartilage thickness of 1 mm] in the width of the cartilage defect.
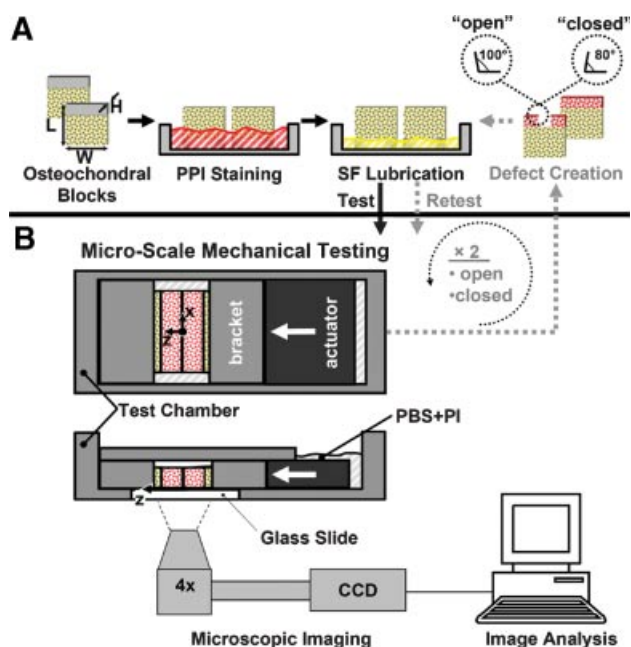
Microscale Mechanical Testing
Mechanical testing was performed in a microscope-mounted test chamber, as described previously (Fig. 1B).[31,32,34,35] Briefly, pairs of blocks were positioned with their articular surfaces opposing and aligned perpendicular to the direction of loading (z-axis). Tissue deformation was imaged through the glass chamber bottom (x–z plane) using a Nikon Diaphot 300 epi-fluorescence microscope fitted with a G-2A filter cube (Nikon, Melville, NY). Samples were imaged at $4\times$ magnification ($\sim1.8 \times 2.8$ cm^2 field of view) and digital images (512×768 pixels; 8-bit grayscale) were recorded with a charge-coupled device camera (Model 4913-5000, Cohu, Inc., San Diego, CA). Samples were loaded under uniaxial unconfined compression to a total bone-to-bone strain of 20% (defined as the applied displacement/sum of the cartilage thicknesses), at a strain rate of $1\% \cdot s^{-1}$ using a displacement controlled actuator (Model MFN25PP, Newport Corporation, Irvine, CA). Digital images of the contacting surfaces (centered at the defect rim where applicable) were acquired directly prior to loading, during loading at a rate of four frames/s (8 µm applied displacement/frame), directly following loading, and during stress relaxation (30-s intervals between 1 and 6 min after loading, and then at 10, 15, 30, and 60 min).

Image and Data Analysis
Indices of the biomechanics of cartilage contact were obtained from the acquired images. Macroscopic changes in deformation of the opposing tissue surfaces and sliding behavior were observed qualitatively. Tissue deformation and sliding were quantified from digital images, as described previously,[36] using a custom program written for MATLAB 6.5 with functions from the Image Processing Toolbox (Mathworks, Inc., Natick, MA).

Tissue deformation was quantified by tracking the movement of both interior points and the contacting surfaces. A subset of fluorescently stained cell nuclei, spaced at approximately 15 pixels (~55 µm), served as fiducial markers of material points in digital images of the tissue during loading and stress relaxation. The translation of each point was tracked through each frame by iteratively maximizing normalized cross-correlation with both the preceding and initial frames. The boundaries of the two surfaces were defined by manually selecting points along each surface in the initial frame and then automatically tracked through subsequent frames.

Width-averaged intensity versus axial (z-) position profiles were calculated for 100 pixel wide (x-direction) × length of the image (z-direction) rectangular regions around each surface point. Axial positions of surface points were then adjusted at each frame to minimize the squared error terms between the current intensity and intensity gradient profiles and those of the previous frame. The gross accuracy of surface tracking was manually verified in each frame; if surface tracking was lost, points were manually repositioned and tracking was restarted from that point.

Mesh points were defined at 100 μm spacing in the manually selected region of interest (ROI) and used to calculate tissue displacements, displacement gradients, Lagrangian strains, area changes, and surface sliding. At each time point, the positions of mesh points not along the articular surface were updated using a local affine mapping of the surrounding tracked nuclei (typically 16 nuclei; 200×200 μm region); lateral positions of mesh points at the articular surface were determined similarly, with axial positions determined from the tracked surface. Poorly correlated fiducial markers were excluded from these calculations. If correlation was low for the entire region, the mesh point was adjusted using a mapping of the surrounding mesh points.

Intratissue deformations were determined from mesh point displacements. In-plane displacement gradients were calculated at each mesh point using finite-difference calculations. Lagrangian strains were then calculated from those displacement gradients, and the finite in-plane area change, dA–dA$_0$, at each point was calculated relative to the initial area, dA$_0$, as:

$$\frac{dA - dA_0}{dA_o} = \left(1 + \frac{\partial u}{\partial x}\right)\left(1 + \frac{\partial w}{\partial z}\right) - \frac{\partial u}{\partial z}\frac{\partial w}{\partial x} - 1 \quad (1)$$

To quantify sliding, the positions of points along both tissue surfaces (100 μm spacing) were tracked dynamically during loading.[36] One surface was chosen as the slave surface and at each frame, the projection of each point on that surface onto the opposing master surface was determined. The relative displacement of the slave point with respect to the master surface was determined over each time step and separated into components parallel (sliding) and perpendicular (gap velocity) to the master surface.

Local sliding distances were then determined, considering the tendency for a specific pair of blocks to slide preferentially (in either direction), as well as to be affected locally by the defect. Thus, total sliding was assumed to represent, a combination of (1) general sliding between a particular pair of blocks, which may take place in either direction and is present over the entire surface, even, far (>1.5 mm) from the defect, and (2) defect-related sliding in the local region (within 1 mm) of the defect, with the adjacent cartilage moving toward the defect with respect to the opposing surface (Fig. 2). The general sliding between two blocks was estimated as the average relative lateral displacement (RLD) occurring between the two intact blocks, calculated from the lateral displacements of points on the opposing surfaces that were adjacent prior to loading. Differential sliding was calculated as the locally tracked total sliding, less the RLD, for points along surfaces of that same pair of blocks in each sample configuration (intact, "open" defect, and "closed" defect). All sliding data are reported as these differential values, representing the local effects of the defect.
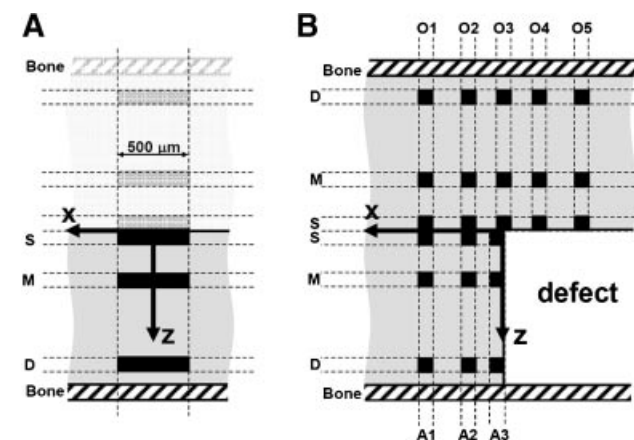
Statistics
Data are presented as mean ± SEM, unless otherwise noted. Strain and deformation data are graphed with higher bars
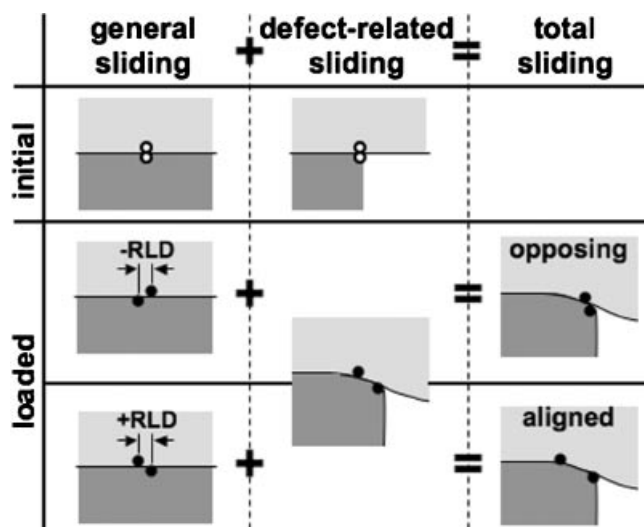
Figure 2. Schematic of sliding components combining to determine the sliding measured near a defect. Open circles show representative points prior to loading, while solid circles indicate the deformed positions of those points following loading. General sliding between intact blocks can occur in either direction, effectively supplementing or reducing the localized sliding induced by the defect, which always occurs in the same direction.

representing increased magnitudes in the predominant form of strain (i.e., negative, compressive strains for E_{zz} and positive, tensile strains for E_{xx}). For tests of opposing intact surfaces, data from the two opposing surfaces were pooled to provide one set of strain measurements (at S, M, and D depths) per sample pair (Fig. 3A). For defect-containing blocks, several lateral locations along the adjacent and opposing cartilage surfaces (Fig. 3B) were analyzed. All data were log transformed before analysis to adjust for sample variances that were proportional to amplitude. Statistical analyses ($\alpha = 0.05$) were performed using Systat 10.2.05 (Systat Software, Richmond, CA) and Microsoft Office Excel 2003 (Microsoft Corporation, Redmond, WA).

Figure 3. Locations of subregions used for statistical analysis of strain distributions in (A) intact control and (B) defect-containing samples. Comparisons were made at three tissue depths: S {$z = 0$ to 100 μm}, M {$z = 300$ to 400 μm}, D {$z = 900$ to 1000 μm}. For intact controls, a 500-μm width region was averaged as a control strain for each depth. For defect samples, 100×100 μm² subregions were analyzed for S, M, and D depths at select lateral locations on the adjacent (A1 {$x = 500$ to 600 μm}; A2 {$x = 200$ to 300 μm}; A3 {$x = 0$ to 100 μm}) and opposing (O1 {$x = 500$ to 600 μm}; O2 {$x = 200$ to 300 μm}; O3 {$x = -50$ to 50 μm}; O4 {$x = -200$ to -300 μm}; O5 {$x = -500$ to -600 μm}) cartilage surfaces.

The time course of strain and area changes were analyzed over two separate time periods: during loading and during relaxation. First, effects of "open" versus "closed" defects were compared (data not shown) in two four-way ANOVAs with defect type, tissue depth (S, M, D), surface location (eight groups: A1–A3 and O1–O5) as factors, and time (representing either applied compression or relaxation time) as a repeated factor. Analyses showed no effect of defect type on any strain component during loading ($|E_{xz}|$, $p = 0.18$; E_{xx}, $p = 0.23$; E_{zz}, $p = 0.38$) or relaxation ($|E_{xz}|$, $p = 0.47$; E_{xx}, $p = 0.28$; E_{zz}, $p = 0.76$). Because no effect of defect type was seen, strain data from "open" and "closed" defects were pooled for subsequent analyses (comparisons between defect and intact control samples), to provide a single strain distribution per sample pair.

Using pooled strain data, the overall effects of tissue depth (S, M, D), defect presence/surface location (nine groups: C, A1–A3, O1–O5), and time (representing either applied compression or relaxation time) were analyzed by a three-way ANOVA, with tissue depth and time as repeated factors. Regional variations in strain were analyzed in detail at two specific time-points: (1) postloading and (2) postrelaxation. Planned comparison (a priori) t-tests (for uneven variances) were used to compare the values of strain at each position (S, M, and D depths at locations A1–A3 and O1–O5) along the adjacent and opposing surfaces to the intact control value (C) at the same depth.

The differential sliding distances over surface points were analyzed at four time points during loading (corresponding to applied compressions of approximately -0.05, -0.10, -0.15, and -0.20). At each time point, planned (a priori) comparisons were used to compare sliding at points along the surface adjacent to the defect ($x = 0, 100, 200, 300, 400,$ and $500\,\mu m$; for both defect configurations), to the average sliding over the central region of intact control samples ($x = -250$ to 250). For each sample, the average sliding distance over the analyzed 500-μm surface region (adjacent to the defect or in the center of intact samples) was also calculated at each of the four time points. The overall effects and interactions of defect presence and level of applied compression (time point) were analyzed by two-way ANOVA with applied compression (time) as a repeated factor. Average sliding distances at each time point were then normalized to the approximate applied axial displacement at that time, and the average value over those four times was calculated, representing the normalized sliding distance of the sample. The average normalized sliding distance for the $n = 4$ sample pairs was calculated in the intact, "open" defect, and "closed" defect configurations, and these values were analyzed by ANOVA with a Tukey post hoc test.

RESULTS

Overall, there were significant effects ($p < 0.001$) of tissue depth, surface location, and applied compression (loading time), on both E_{zz} and $|E_{xz}|$ magnitudes during the loading period (data not shown for intermediate time points). All first-order ($p < 0.001$) and second-order ($p < 0.05$) interactions between these factors were also significant, indicating that the effects of defects were not experienced equally at all tissue depths and that the time course of strain development during loading depended on both tissue depth and the lateral location with respect to a defect. E_{xx} magnitudes were significantly affected by applied compression, surface location, and their interaction ($p < 0.001$), but were not detectably altered by tissue depth ($p = 0.12$).

In intact samples, strains were initially most evident in the superficial region, reaching local compressive magnitudes of approximately -0.10 before noticeable deformation of the middle or deep regions. As loading was continued, strains in the superficial region continued to rise, but middle and deep regions also began to accumulate measurable levels of strain. Directly following loading, there was a depth-dependent distribution of axial compressive strain (Fig. 4), with high strains, -0.31 ± 0.02, in S, moderate strains, -0.18 ± 0.04, in M, and low levels of strain, -0.03 ± 0.01, in D. Magnitudes of E_{xx} and $|E_{xz}|$ strains rose slightly during loading but remained low, generally staying below 0.05 at all depths and time points.

Cartilage surrounding a defect (Figs. 4 and 5) experienced increased compressive E_{zz}, tensile E_{xx}, and $|E_{xz}|$. In the adjacent cartilage, strain was again initially carried in the S region, but in addition to axial compression, there was an early onset of tensile E_{xx} and increased $|E_{xz}|$ as the adjacent cartilage began to bow into the defect region. As loading proceeded, strain rose more quickly in the S and M regions of adjacent cartilage, than in the corresponding regions of intact control samples. As the peak displacement was reached, E_{zz} at the defect rim (A3-S) and $|E_{xz}|$ in much of the adjacent cartilage were significantly elevated compared to controls (Fig. 4; $p < 0.05$). For the opposing surface, regions remaining in contact with the adjacent surface (O1–O3) had patterns of E_{zz} similar to intact controls. Increased $|E_{xz}|$ ($p < 0.05$) was experienced in the S and D regions of tissue opposing the defect rim (O3) and in the neighboring (O2,O4) D regions. Noncontacting regions (O4,O5) experienced significantly lower E_{zz} than controls ($p < 0.05$) and slight compressive E_{xx} ($p < 0.05$).

During stress relaxation, axial strains were significantly affected ($p < 0.001$) by surface location, tissue depth, and relaxation time, with significant interactions between relaxation time and both surface location and depth. E_{xx} and $|E_{xz}|$ were significantly affected by surface location ($p < 0.001$), tissue depth ($p < 0.05$), and their interaction ($p < 0.05$), but showed no effect of relaxation time ($p > 0.30$) or its interactions ($p > 0.08$).

As intact samples relaxed, the cartilage quickly began to redistribute strain into the S and M layers. In the fully relaxed state, axial strain decreased significantly with depth ($p < 0.05$). Axial compression averaged -0.36 ± 0.01 in the S region and -0.27 ± 0.03 in the M region, whereas compression in the D region was minimal ($|E_{zz}| < 0.05$). E_{xx} and $|E_{xz}|$ magnitudes remained low at all tissue depths, not exceeding 0.05.

As defect samples relaxed, the strains in the tissue adjacent to and opposing the defect quickly approached equilibrium (within 6 min postloading), similar to control samples. In the relaxed state, axial strains in S, M, and D regions of the adjacent cartilage were no longer significantly different than control values. However, significantly elevated $|E_{xz}|$ was still present at the defect rim (A3-S; $p < 0.05$). Interestingly, there was also a strong trend ($p = 0.057$ and $p = 0.053$ after loading and elaxation, respectively) toward increased lateral
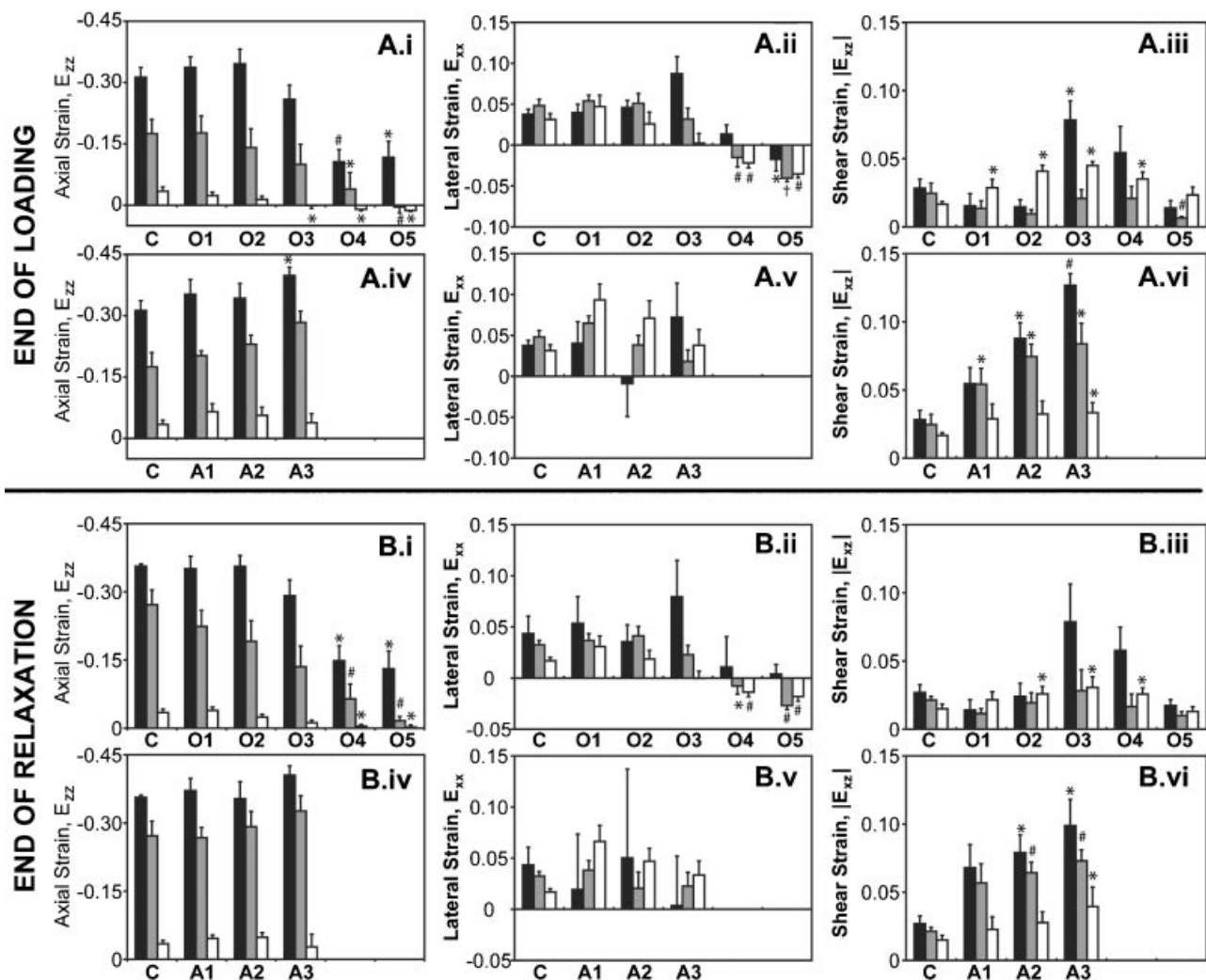
Figure 4. Strain measurements at selected subregions at time points directly following loading (A.i–A.vi) and after stress relaxation for 1 h (B.i–B.vi). Strains were calculated in $100 \times 100 \; \mu m^2$ subregions at S (■), M (▨), and D (□) depths for several lateal positions along the cartilage surfaces adjacent (A1–A3) and opposing (O1–O5) a focal defect; strain data are presented in the relative physical locations where they appear in the images (and Fig. 3), with increasing numbers (1–5) indicating movement parallel to the articular surface and contacting regions across from each other (i.e., A1, A2, and A3) are beneath O1, O2, and O3, respectively, while O4 and O5 are over an empty region. Strain in each subregion was compared to the value from intact control samples (C) at the corresponding depth (*$p < 0.05$; #$p < 0.01$;, †$p < 0.001$). Data are expressed as mean ± SEM. $n = 4$.
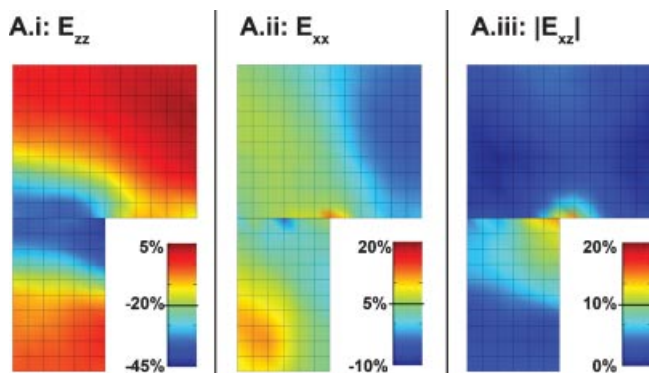
**Figure 5.** Composite strain maps showing regions surrounding a defect, ± 600 μm laterally from the defect and 1 mm depth, directly following loading (see electronic supplement for strain maps following relaxation). Boxes = $100 \times 100 \; \mu m^2$. $n = 4$.

tension in the D regions of the adjacent cartilage (A1-D), seemingly resisting the bending of the adjacent cartilage into the defect area. For the opposing surface, axial and lateral strains in contacting regions were similar to controls. $|E_{xz}|$ returned to normal in the region contacting the defect rim (O3-S), but remained elevated in the D regions (O2–O4). The significantly lower axial strains ($p < 0.05$) and slight lateral compression ($p < 0.05$), noted earlier, remained in the noncontacting regions after relaxation (O4,O5).

The time courses and distributions of area changes (Fig. 6) closely resembled those of E_{zz}, with substantial compaction (>25% area loss) of tissue near the articular surface directly after loading. Area loss was significantly affected by surface location, tissue depth, time, and their first-order interactions during both loading and relaxation periods ($p < 0.01$). Area changes decreased with
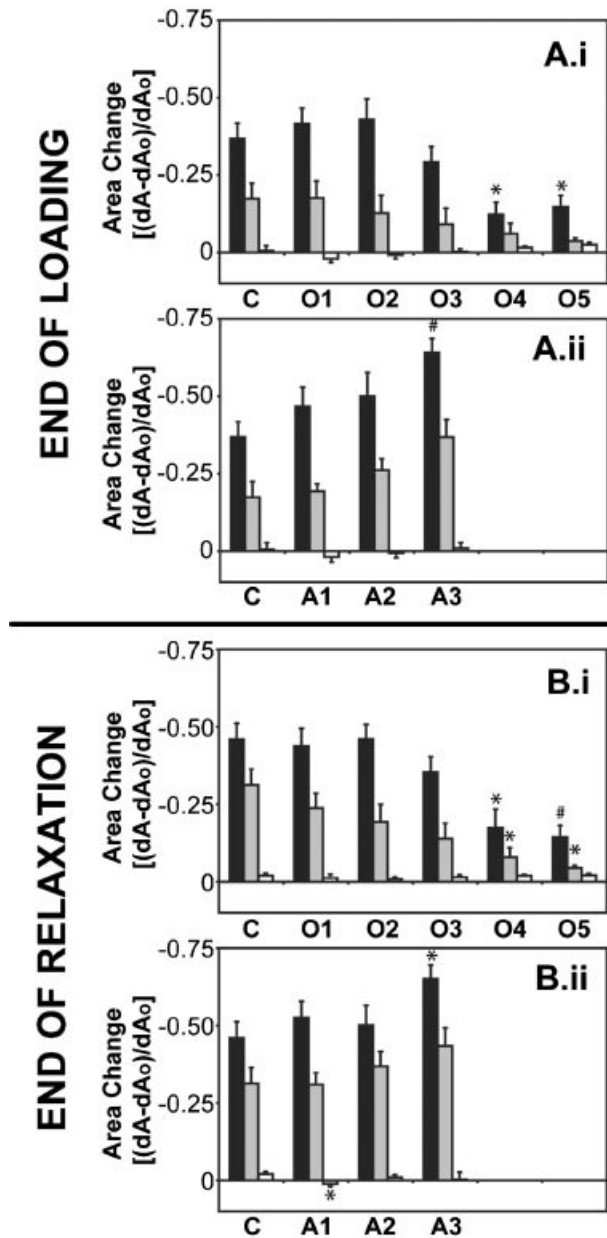
Figure 6. Area changes at selected subregions at time points directly following loading (A.i–A.ii) or after stress relaxation (B.i–B.ii). Strains were calculated in $100 \times 100 \ \mu m^2$ subregions at S (■), M (▦), and D (□) depths for several lateral positions along the cartilage surfaces adjacent (A1–A3) and opposing (O1–O5) a focal defect. Strain data are presented in the relative physical locations where they appear in the images (and Fig. 3). Strain in each subregion was compared to the value from intact control samples (C) at the corresponding depth (*$p < 0.05$; #$p < 0.01$). Data are expressed as mean ± SEM. $n = 4$.

tissue depth and were negligible in the deep regions. During relaxation, the magnitudes of area loss increased almost two-fold in the S and M regions of intact control surfaces, while the D region tissue remained approximately uncompressed. In defect samples, significantly greater area loss, -0.64 ± 0.04, was measured at the defect rim, than in the S regions of intact controls (-0.37 ± 0.05) directly following loading ($p < 0.05$). Unlike intact samples, tissue area at the defect rim was relatively constant during stress relaxation, but

remained higher than controls in the relaxed state ($p < 0.05$).

Average sliding distances increased with greater applied compression ($p < 0.001$) and differed significantly between sample types ($p < 0.05$), with significant interaction between those two factors. Sliding distance was affected by the presence and edge orientation (closed: $79.5 \pm 3.5°$; open: $98.8 \pm 3.0°$) of a defect (Fig. 7),
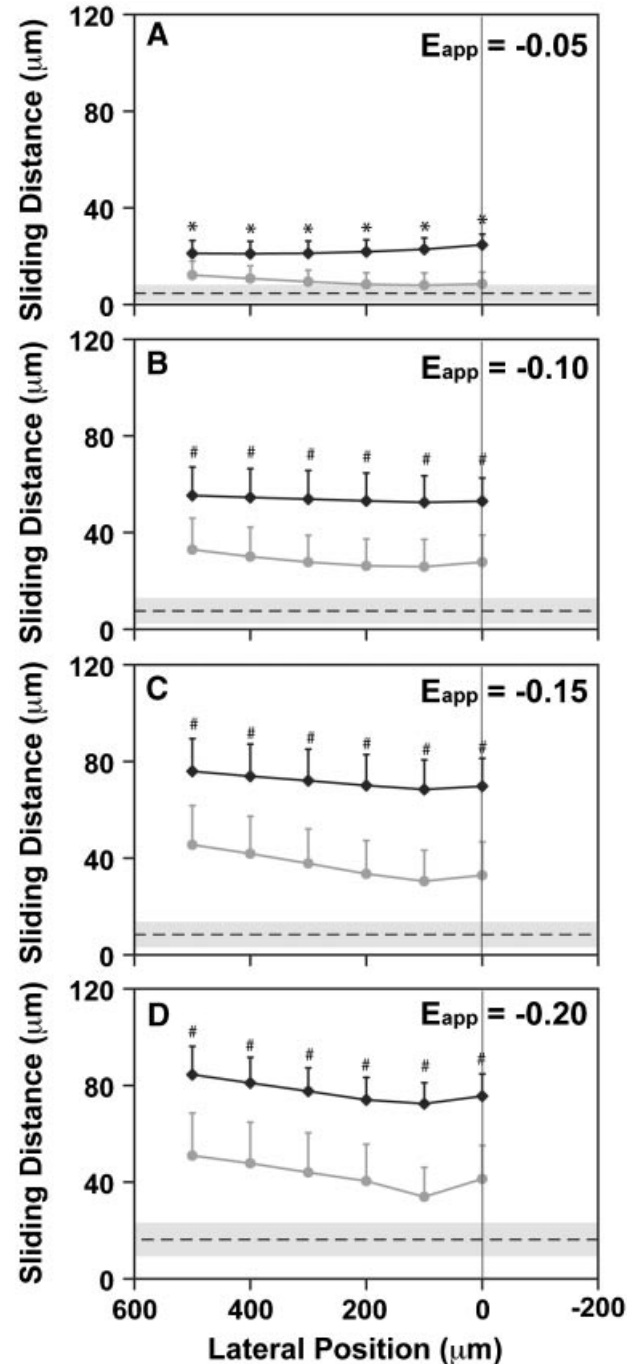
Figure 7. Differential sliding distance profiles over surfaces adjacent to open defects (gray line) and closed defects (black line), compared to the average sliding over intact surfaces (mean: dotted line; SEM: shaded region) at several levels of applied compression (-0.05, -0.10, -0.15, and -0.20). (*$p < 0.05$; #$p < 0.01$, compared to control at the same time point). Data are expressed as mean ± SEM. $n = 4$.

with increased sliding near "closed" defects at all analyzed time points ($p < 0.05$). "Open" defect orientations resulted in a trend toward increased sliding, but no statistically significant increases compared to controls. Normalized sliding distances adjacent to "closed" defects, 0.31 ± 0.06, were significantly greater ($p < 0.05$) than controls, 0.05 ± 0.03, but were not significantly increased near "open" defects, 0.16 ± 0.06 ($p = 0.37$).
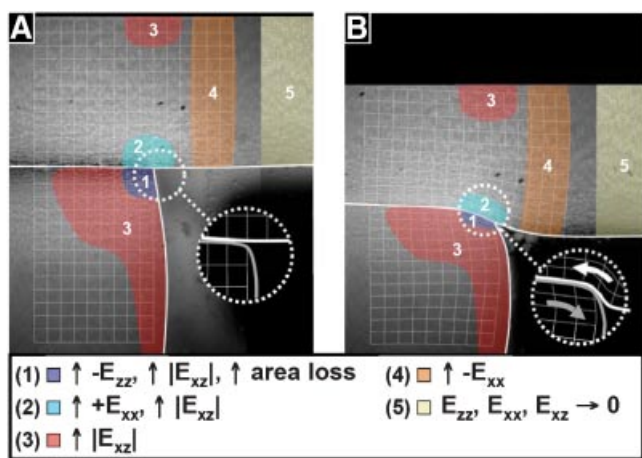
DISCUSSION

This study quantified the dynamic biomechanics of articular cartilage occurring in the vicinity of a focal full-thickness defect, both within the cartilage tissue and in terms of sliding between naturally lubricated articular cartilage surfaces. The results indicate that defect presence has dramatic effects on dynamic cartilage deformation and that defect presence and edge characteristics influence the sliding between articular cartilage surfaces (Fig. 8). During contact between intact surfaces, the superficial region compressed first and axial strains spread into deeper tissue regions at higher levels of compression. As the tissue was allowed to stress relax in the compressed state, strain in the deep tissue redistributed to the middle and superficial tissue regions. Defects with both "open" and "closed" orientations affected strain distributions similarly. Tissue adjacent to a defect experienced increased magnitudes of axial, lateral, and shear strain. During stress relaxation, axial strain distributions returned to levels similar to that displayed by intact surfaces, but elevated shear and lateral tensile strains were maintained. Slightly elevated shear strains and regions of lateral compression occurred in the tissue opposing the defect rim, and strains dissipated in tissue over

Figure 8. Summary of mechanical changes occurring in the regions adjacent to (bottom) and opposing (top) a focal defect during loading. Regions with altered deformation states (compared to the corresponding depths in normal, intact blocks in compression) are mapped to images of a representative defect sample in both the initial (A) and deformed (B) states; meshes overlaid on the images show the transition of uniform 100 μm^2 regions (A) into their deformed states (B) for the analyzed regions of interest (Fig. 3) of this representative sample. Schematics of the defect rim (dotted circles) depict typical deformation and direction of sliding (arrows) between the opposing surfaces. Trends were the same for both defect orientations.

the empty defect area. Increased sliding occurred near defects with "closed" orientations, but not "open" orientations.

The raw values of strain and sliding distance magnitudes measured here may be influenced by the some of the chosen experimental parameters (discussed in detail below), but the relative distributions of strain components (showing regions in tension vs. compression, low vs. high magnitudes), changes in strain magnitudes and time-courses, and the general sliding behavior should be preserved. These findings can be used to predict tissue regions that are most at risk for damage due to high strains, tissue compaction, or increased sliding, independent of the absolute values of the measured strains.

The mechanical behavior of a focal defect is likely to depend markedly upon its size, shape, and location in the joint, as well as the way in which loading occurs. In the current study, the in vitro parameters of defect geometry and boundary conditions addressed particular defect and loading situations; such factors are likely to have significant effects on the time courses of strain development and relaxation. Clinically observed focal defects have been noted to be larger than 1 cm^2 in area for >80% of defects and larger than 2 cm^2 in area for >50% of defects.[2] These areas approach or exceed typical contact areas (~2–3 cm^2 for a single compartment) in tibio-femoral articulation.[39] For large, irregularly shaped defects on curved surfaces, as well as focal defects that are not completely within the contact area, loading will therefore often occur on only a portion of the defect. With a partially loaded, full-thickness defect area, fluid depressurization will be allowed through the subchondral bone and due to the lack of "sealing" at the rim. The chosen in vitro defect geometry was a full-thickness slot in a cartilage block, a configuration that allows clear viewing of a defect edge and also does not constrain the lateral edges of cartilage tissue. This configuration provides a good model of the deformation expected at a partially loaded defect. The current test configuration also allowed fluid depressurization through the slot and sides of the tissue, consistent with the specified type of defect. The current model is less applicable to smaller defects that are completely covered by the opposing surface during loading and also partial-thickness defects that do not extend to the subchondral bone. In those defects, a significant hoop stress would develop around the defect rim that would help resist deformation, and fluid depressurization would not occur through the subchondral bone or over the defect rim. Thus, although the present study provides analysis of one set of controlled biomechanical boundary conditions, others remain to be investigated.

A conservative loading protocol was used to establish a baseline for the effects of a focal defect. Loading consisted of uniaxial compression, applied in displacement control at a constant strain rate, and with intact and defect-containing samples compressed to the same total bone-to-bone strain. This loading is simplified

compared to the in vivo environment, which would include both lateral and axial components and where strain and strain rates would depend upon the joint loading during articulation. Alternatively, very large samples could be compressed with the same total load; there, contact stress near the defect would be increased with the lost contact area and a portion of the load would be redistributed to normally unloaded areas. However, that situation would involve additional experimental challenges of detailed analysis of curvature and contact over large areas. Given the conservative parameters used in the current study, it is notable that significant local strain and sliding magnitudes (which both increased significantly with increasing applied compression) were still measured. The applied strain rate $(1\% \cdot s^{-1})$ was chosen to fall below the threshold known to induce acute tissue damage, but still be representative of an instantaneous loading response.[40,41]

Axial compressive strains in intact control samples decreased significantly with tissue depth, similar to previous reports.[31–34] However, direct comparisons to those studies are complicated by differences in test parameters (e.g., presence or absence of underlying bone, unconfined vs. confined compression, relaxation time, and tissue source). Strain data are presented for the current, geometrically motivated, set of axes (as opposed to principal strains), because in a highly anisotropic tissue like cartilage, both the magnitudes and orientations of strains relative to the articular cartilage structure may be important. Graphs of the minimum and maximum principal strains and the maximum shear strains are included in the electronic supplement. The behavior of defect samples in this study was also consistent with previous observations. Macroscopic tissue deformation near defects was similar to that reported previously,[28] where the tissue adjacent to defects loaded in ex vivo joints began to collapse inward into the defect and opposing tissue bulged into to empty region. This partial collapse of tissue at the defect rim, along with the slightly lower compression in the tissue opposing it, may also help explain the results of contact stress studies that showed decreased contact stresses directly at the defect rim.[26]

A variety of factors may have contributed to the increased sliding that occurred at the defect rim of defects with "closed" orientations at all analyzed time points. High variability between individual samples suggests that other factors, such as surface curvature, may also contribute to sliding behavior. Defects with "open" orientations resulted in little or no increased sliding, but may expose the radial edge of the defect to sliding; that surface does not normally experience contact, and may be less wear resistant than the articular surface. It remains unclear if either geometry is preferable or detrminental in vivo, although defects cut at large "open" angles (135°) have been correlated to poor in vivo repair outcomes.[42]

The increased strain, tissue area loss, and surface sliding present at the defect rim may directly contribute to defect progression through multiple mechanobiological mechanisms. Even under a conservative loading protocol, time courses of strain development were affected and local strains exceeded magnitudes shown to cause cartilage damage.[9,11,13–15,17] The presence of a defect also influences several of the parameters known to mediate the processes of wear and fatigue,[23] including the applied normal stress, surface lubrication, friction, sliding path length, and the characteristics of the contacting surfaces. The accelerated tissue relaxation observed in the current study is consistent with fluid depressurization near the defect edge, potentially altering the lubrication regime and increasing friction. Defect presence also induced additional sliding that, even at magnitudes much lower than sliding due to joint articulation, may be significant because they occur in the regions that likely have elevated contact stresses. The presence of a defect, especially one with an "open" orientation, may also result in articulation of regions, such as the defect edges, that do not normally experience sliding and may be less wear resistant than the articular surface. These factors could all contribute to significantly accelerated rates of wear and fatigue over long-term loading, even in the absence of acute tissue damage.

Effects of focal defects on the mechanical environment of articular cartilage could also significantly affect the response of the indwelling cells. Mechanically induced cell damage or tissue loss could reduce the cell population, compromising the overall biosynthetic response of the tissue.[43] In addition, the remaining viable cells may have altered metabolic function after experiencing strains that reach injurious levels.[9,15] In general, changes in the static and dynamic strain state of the tissue may regulate the cellular and matrix processes involved in tissue repair and remodeling.[25,44] The relationship between the mechanical consequences of defects determined here and these potential adverse cellular effects has yet to be investigated, and could provide insights into disease progression.

ACKNOWLEDGMENTS

REFERENCES

1. Curl WW, Krome J, Gordon ES, et al. 1997. Cartilage injuries: a review of 31,516 knee arthroscopies. Arthroscopy 13:456–460.
2. Hjelle K, Solheim E, Strand T, et al. 2002. Articular cartilage defects in 1,000 knee arthroscopies. Arthroscopy 18:730–734.
3. Cicuttini F, Ding C, Wluka A, et al. 2005. Association of cartilage defects with loss of knee cartilage in healthy, middle-age adults: a prospective study. Arthritis Rheum 52:2033–2039.
4. Wang Y, Ding C, Wluka AE, et al. 2006. Factors affecting progression of knee cartilage defects in normal subjects over 2 years. Rheumatology (Oxford) 45:79–84.

5. Wluka AE, Ding C, Jones G, et al. 2005. The clinical correlates of articular cartilage defects in symptomatic knee osteoarthritis: a prospective study. Rheumatology (Oxford) 44: 1311–1316.

6. Jackson DW, Lalor PA, Aberman HM, et al. 2001. Spontaneous repair of full-thickness defects of articular cartilage in a goat model. A. preliminary study. J Bone Joint Surg Am 83-A: 53–64.

7. Lefkoe TP, Trafton PG, Ehrlich MG, et al. 1993. An experimental model of femoral condylar defect leading to osteoarthrosis. J Orthop Trauma 7:458–467.

8. Jeffrey JE, Gregory DW, Aspden RM. 1995. Matrix damage and chondrocyte viability following a single impact load on articular cartilage. Arch Biochem Biophys 322:87–96.

9. Quinn TM, Allen RG, Schalet BJ, et al. 2001. Matrix and cell injury due to sub-impact loading of adult bovine articular cartilage explants: effects of strain rate and peak stress. J Orthop Res 19:242–249.

10. Wilson W, van Burken C, van Donkelaar C, et al. 2006. Causes of mechanically induced collagen damage in articular cartilage. J Orthop Res 24:220–228.

11. Thibault M, Poole AR, Buschmann MD. 2002. Cyclic compression of cartilage/bone explants in vitro leads to physical weakening, mechanical breakdown of collagen and release of matrix fragments. J Orthop Res 20:1265–1273.

12. Radin EL, Burr DB, Caterson B, et al. 1991. Mechanical determinants of osteoarthritis. Semin Arthritis Rheum 21: 12–21.

13. D'Lima DD, Hashimoto S, Chen PC, et al. 2001. Cartilage injury induces chondrocyte apoptosis. J Bone Joint Surg Am 83-A (Suppl 2):19–21.

14. Loening A, Levenston M, James I, et al. 2000. Injurious mechanical compression of bovine articular cartilage induces chondrocyte apoptosis. Arch Biochem Biophys 381:205–212.

15. Kurz B, Jin M, Patwari P, et al. 2001. Biosynthetic response and mechanical properties of articular cartilage after injurious compression. J Orthop Res 19:1140–1146.

16. Clements KM, Bee ZC, Crossingham GV, et al. 2001. How severe must repetitive loading be to kill chondrocytes in articular cartilage? Osteoarthritis Cartilage 9:499–507.

17. Patwari P, Gaschen V, James IE, et al. 2004. Ultrastructural quantification of cell death after injurious compression of bovine calf articular cartilage. Osteoarthritis Cartilage 12: 245–252.

18. Bae WC, Schumacher BL, Sah RL. 2007. Indentation probing of human articular cartilage: effect on chondrocyte viability. Osteoarthritis Cartilage 15:9–18.

19. Weightman B. 1976. Tensile fatigue of human articular cartilage. J Biomech 9:193–200.

20. Weightman B, Chappell DJ, Jenkins EA. 1978. A second study of tensile fatigue properties of human articular cartilage. Ann Rheum Dis 37:58–63.

21. Bellucci G, Seedhom BB. 2001. Mechanical behaviour of articular cartilage under tensile cyclic load. Rheumatology (Oxford) 40:1337–1345.

22. Lipshitz H, Glimcher MJ. 1979. In vitro studies of the wear of articular cartilage. II. characteristics of the wear of articular cartilage when worn against stainless steel plates having characterized surfaces. Wear 52:297–339.

23. Ateshian GA, Mow VC. 2005. Friction, lubrication, and wear of articular cartilage and diarthrodial joints. In: Mow VC, Huiskes R, Mow VC, Huiskes RS, editors. Basic orthopaedic biomechanics and mechano-biology. 3rd ed. Philadelphia, PA: Lippincott Williams & Wilkins; p 447–494.

24. Sah RL, Kim YJ, Doong JH, et al. 1989. Biosynthetic response of cartilage explants to dynamic compression. J Orthop Res 7:619–636.

25. Guilak F, Sah RL, Setton LA. 1997. Physical regulation of cartilage metabolism. In: Mow VC, Hayes WC, Mow VC, Hayes WCS, editors. Basic orthopaedic biomechanics. 2nd ed. New York: Raven Press; p 179–207.

26. Brown TD, Pope DF, Hale JE, et al. 1991. Effects of osteochondral defect size on cartilage contact stress. J Orthop Res 9:559–567.

27. Guettler JH, Demetropoulos CK, Yang KH, et al. 2004. Osteochondral defects in the human knee: influence of defect size on cartilage rim stress and load redistribution to surrounding cartilage. Am J Sports Med 32:1451–1458.

28. Braman JP, Bruckner JD, Clark JM, et al. 2005. Articular cartilage adjacent to experimental defects is subject to atypical strains. Clin Orthop Relat Res 430:202–207.

29. Ateshian GA, Wang H. 1995. A theoretical solution for the frictionless rolling contact of cylindrical biphasic articular cartilage layers. J Biomech 28:1341–1355.

30. Pena E, Calvo B, Martinez MA, et al. 2007. Effect of the size and location of osteochondral defects in degenerative arthritis. A. finite element simulation. Comput Biol Med 37:376–387.

31. Schinagl RM, Ting MK, Price JH, et al. 1996. Video microscopy to quantitate the inhomogeneous equilibrium strain within articular cartilage during confined compression. Ann Biomed Eng 24:500–512.

32. Schinagl RM, Gurskis D, Chen AC, et al. 1997. Depth-dependent confined compression modulus of full-thickness bovine articular cartilage. J Orthop Res 15:499–506.

33. Wang CC, Deng JM, Ateshian GA, et al. 2002. An automated approach for direct measurement of two-dimensional strain distributions within articular cartilage under unconfined compression. J Biomech Eng 124:557–567.

34. Bae WC, Lewis CW, Levenston ME, et al. 2006. Indentation testing of human articular cartilage: effects of probe tip geometry and indentation depth on intra-tissue strain. J Biomech 39:1039–1047.

35. Klein TJ, Chaudhry M, Bae WC, et al. 2007. Depth-dependent biomechanical and biochemical properties of fetal, newborn, and tissue-engineered articular cartilage. J Biomech 40:182–190.

36. Gratz KR, Sah RL. 2008. Experimental measurement and quantification of frictional contact between biological surfaces experiencing large deformation and slip. J Biomech 41:1333–1340.

37. Wong BL, Bae WC, Chun J, et al. 2008. Biomechanics of cartilage articulation: effects of lubrication and degeneration on shear deformation. Arthritis Rheum 58:2065–2074.

38. Frank EH, Grodzinsky AJ, Koob TJ, et al. 1987. Streaming potentials: a sensitive index of enzymatic degradation in articular cartilage. J Orthop Res 5:497–508.

39. Patel VV, Hall K, Ries M, et al. 2004. A three-dimensional MRI analysis of knee kinematics. J Orthop Res 22:283–292.

40. Mow VC, Kuei SC, Lai WM, et al. 1980. Biphasic creep and stress relaxation of articular cartilage in compression: theory and experiment. J Biomech Eng 102:73–84.

41. Frank EH, Grodzinsky AJ. 1987. Cartilage electromechanics-I. Electrokinetic transduction and the effects of electrolyte pH and ionic strength. J Biomech 20:615–627.

42. Rudd RG, Visco DM, Kincaid SA, et al. 1987. The effects of beveling the margins of articular cartilage defects in immature dogs. Vet Surg 16:378–383.

43. Hunziker EB, Quinn TM. 2003. Surgical removal of articular cartilage leads to loss of chondrocytes from cartilage bordering the wound edge. J Bone Joint Surg Am 85-A (Suppl 2):85–92.

44. Grodzinsky AJ, Levenston ME, Jin M, et al. 2000. Cartilage tissue remodeling in response to mechanical forces. Annu Rev Biomed Eng 2:691–713.